Appl Phys B (2010) 101: 79–91
DOI 10.1007/s00340-010-4038-2

Applied Physics B
Lasers and Optics

Full parametric pulse shaping in phase, amplitude, and polarization using an effective four-array modulator

F. Weise · A. Lindinger

Received: 19 January 2010 / Revised version: 12 April 2010 / Published online: 15 July 2010

Abstract We present an analytical method for generating ultra-fast pulse sequences. In this approach, the physically intuitive parameters of the sub-pulses—energy, position in time, relative phase, chirp, and the polarization state—can be controlled individually. The pulses are experimentally generated by a pulse shaper which has been recently introduced. It uses three commercial double liquid crystal array modulators to mimic the optimal setup which utilizes four liquid crystal arrays for modulation. A series of double pulses systematically demonstrates the separate and independent control of the sub-pulse parameters. Furthermore, complex multi-pulse sequences are shown.

1 Introduction

The invention of femtosecond lasers and the development of pulse shaping techniques opened the wide field of coherent control [1, 2]. The implementation of a pulse shaper into a feedback loop makes it possible to find the optimal pulse form for the investigated system without having any knowledge about the underlying physics [3]. By analyzing the obtained pulse shapes, the excitation process can be revealed. This powerful method was applied to many successful experiments in different fields [4].

In these experiments, the pulses were modulated in phase and/or amplitude. Since the majority of quantum systems are three dimensional, the vectorial component of the electrical field, the polarization, has to be considered additionally. Pulse shapers which are capable of polarization shaping were developed. The first attempts at polarization shaping employed standard double liquid crystal arrays which have their optical axes oriented at $\pm 45°$ in the Fourier plane of a 4-f line [5]. The experimental implementation of this setup in a closed-loop experiment on optimizing the ionization of K_2 and I_2 showed nicely the relevance of the vectorial character of the light [6, 7]. Yet, in this setup the polarization control is limited to ellipses with fixed orientation. This limitation was overcome by additionally passing an array with its optical axis parallel to the input polarization in an 8-f geometry [8]. A four-array modulator was used to correct the polarization mode dispersion in optical fibers [9]. However, all these setups are not able to modulate the amplitude of the laser pulse. By passing through a 4-f line twice at different locations of a double liquid crystal modulator, the amplitude of the laser pulse was additionally shaped [10]. The restriction of the polarization control also applies for this setup.

The first setup which provides the full control of the polarization along with phase and amplitude modulation utilizes a pulse shaper incorporated in a Mach–Zehnder interferometer [11]. The idea of this setup is based on superimposing two orthogonally linearly polarized pulses which are shaped in phase and amplitude. The stability of this type of interferometric pulse shaping is a central point and was improved in a common optical setup [12, 13] and by active stabilization [14]. By employing the approach of overlapping two shaped pulses which are perpendicularly polarized, it was also possible to extend the polarization shaping to the mid infrared [15] and to the ultraviolet [16].

Recently, we introduced a modulator which effectively utilizes four liquid crystal arrays to obtain full control over the electrical field of the laser pulse [17]. This modulator is placed in the Fourier plane of a standard 4-f line. Therefore, concerns regarding the stability are irrelevant and the setup

F. Weise (✉) · A. Lindinger
Institut für Experimentalphysik, Arnimallee 14, 14195 Berlin, Germany
e-mail: weise@physik.fu-berlin.de

can be easily aligned. In this paper, we describe an analytical method for generating parametrically tailored multi-pulses with this setup. In this approach, the parameters of each sub-pulse can be modified individually. The full control of the electrical field is essential to achieve this.

This paper is organized as follows. First, in Sect. 2 we present the mathematical basis for the parametrical construction of a pulse sequence, the calculation of the electrical field, and the computation of the individual retardances for the pixel of each array of the modulator. Then, in Sect. 3 we introduce the experimental setup. In Sect. 4 we present the experimental data of a series of double pulses in which one parameter is systematically changed while the others are kept constant. This is followed in Sect. 5 by a selection of complex double pulses in order to show the full scope of parameterization. The capabilities and limitations are discussed in Sect. 6. At the end, in Sect. 7 we consider applications and conclude the paper.

2 Mathematical description

2.1 Parameterization of a pulse sequence

For the construction of the pulse sequence, we used a sub-pulse encoding similar to that in [18]. The parameters intensity (I), position in time, relative phase, and chirp, as well as the polarization state orientation (γ), ellipticity (r), and direction of the helicity of each pulse are individually set. The orientation measures counter clockwise from the x axis and the ellipticity is defined as the ratio of the major axis to the minor axis ($r = A_{\text{major}}/A_{\text{minor}}$) of the ellipse given by the electrical field which is illustrated in Fig. 1. The polarization state of each polarization ellipse is converted to the spectral vectorial components of the electrical field $\tilde{\mathbf{E}}(\omega)$. It is determined by the amplitudes in horizontal (X) and vertical (Y) directions and the phase difference between these spectral components (ϵ). The spectral amplitude in horizontal and vertical directions can be expressed by

$$X = \sqrt{I}\cos\left(\frac{1}{2}\arccos\big(\cos(2\gamma)\cos\big(2\arctan(r)\big)\big)\right), \tag{1}$$

$$Y = \sqrt{I}\sin\left(\frac{1}{2}\arccos\big(\cos(2\gamma)\cos\big(2\arctan(r)\big)\big)\right). \tag{2}$$

The phase difference between the X and Y components determines the ellipticity of the polarization ellipse. It is calculated as

$$\epsilon = \phi_y - \phi_x = \pm\arctan\left(\frac{\tan(2\arctan(r))}{\sin(2\gamma)}\right), \tag{3}$$

in which the sign determines the helicity: plus stands for right-hand polarization and minus for left-hand polarization.

The phase $\Phi(\omega)$ of the sub-pulse is constructed by the spectral Taylor terms b_n. The zero-order term regulates the relative phase between the sub-pulses. It also sets the carrier envelope phase (CEP) if a CEP stabilized laser provides the input pulses. The first-order term b_1 shifts the pulse in time and the quadratic term implies the linear chirp of the sub-pulse, etc. The pulse sequence is composed of the superposition of N sub-pulses. The complex vectorial electrical field in the frequency domain can be written as

$$\tilde{\mathbf{E}}^{\text{par}}(\omega) = \tilde{E}_{\text{in}}(\omega)\sum_N \begin{pmatrix} X_N e^{i\Phi_N(\omega)} \\ Y_N e^{i(\Phi_N(\omega)+\epsilon)} \end{pmatrix} \tag{4}$$

$$= \tilde{E}_{\text{in}}(\omega)\cdot\tilde{\mathbf{H}}^{\text{par}}(\omega), \tag{5}$$

where $\tilde{E}_{\text{in}}(\omega)$ is the electrical field of the incoming linear pulse which serves as a prototype and specifies the available overall pulse energy and spectral width. The calculation of the electrical field can be considered as a multiplication of the incoming electrical field with a modulation function $\tilde{\mathbf{H}}(\omega)$. The modulation function is calculated by

$$\tilde{\mathbf{H}}(\omega) = \frac{\tilde{\mathbf{E}}(\omega)}{\tilde{E}_{\text{in}}(\omega)}. \tag{6}$$

The construction of the modulation function is not restricted to this parameterization. A modulation function of any desired electrical field can be calculated within the limits of the available laser pulses. The electrical field can be obtained by different types of parametrizations or theoretical considerations. A construction of the electrical field in the time domain as $\tilde{\mathbf{E}}(t)$ is also possible, since it is directly connected to the frequency domain $\tilde{\mathbf{E}}(\omega)$ by Fourier transformation. The modulation function is complex and can be expressed by its real and imaginary parts for the horizontal x and vertical y components, respectively:

$$\tilde{\mathbf{H}}(\omega) = \begin{pmatrix} \text{Re}\,H_x^\omega + i\,\text{Im}\,H_x^\omega \\ \text{Re}\,H_y^\omega + i\,\text{Im}\,H_y^\omega \end{pmatrix}. \tag{7}$$

2.2 Calculation of the electrical field produced by the modulator

The modulator which is optimally suited for shaping this kind of pulses consists of four arrays and a polarizer. The configuration of such a modulator could be a sequence of arrays in which the first pair has its optical axes at ±45°, followed by a horizontal polarizer and an array with the optical axes at +45° and 0°. Since such a modulator was not available, we substituted it by a combination of three double liquid crystal modulators with their optical axes at ±45°, a polarizer, and two wave plates, which give the same potential for control. The sequence of the optical components used is a modulator followed by a horizontal polarizer, a second

modulator, and a third modulator which is placed between two half-wave plates at +22.5° (cf. inset of Fig. 1). Other combinations or a different order could also allow for the desired modulation. Details are discussed in [17].

The formula for the electrical field after modulation can be calculated by multiplying the Jones vectors of each optical component with the vector of the incoming field. The electrical field of the four-array modulator is calculated as

$$\begin{aligned}\tilde{\mathbf{E}}_{\text{out}}^{\text{mod}\,4}(\omega_n) &= \tilde{E}_{\text{in}}(\omega_n)\,\mathrm{e}^{\frac{1}{2}\mathrm{i}\left(\varphi_a^{\omega_n}+\varphi_b^{\omega_n}+\varphi_c^{\omega_n}\right)} \\ &\quad\times\cos\left(\frac{\varphi_a^{\omega_n}-\varphi_b^{\omega_n}}{2}\right) \\ &\quad\times\begin{pmatrix}\cos\left(\frac{\varphi_c^{\omega_n}}{2}\right)\\ \mathrm{i}\mathrm{e}^{\mathrm{i}\varphi_e^{\omega_n}}\sin\left(\frac{\varphi_c^{\omega_n}}{2}\right)\sqrt{g}\end{pmatrix} \qquad (8)\\ &= \tilde{E}_{\text{in}}(\omega_n)\cdot\tilde{\mathbf{H}}^{\text{mod}\,4}(\omega_n)\,. \qquad (9)\end{aligned}$$

In the case of the setup used, where three modulators provide a sequence of six arrays, the manipulation of the electrical field can be expressed as

$$\begin{aligned}\tilde{\mathbf{E}}_{\text{out}}^{\text{mod}\,6}(\omega_n) &= \tilde{E}_{\text{in}}(\omega_n)\,\mathrm{e}^{\frac{1}{2}\mathrm{i}\left(\varphi_a^{\omega_n}+\varphi_b^{\omega_n}+\varphi_c^{\omega_n}+\varphi_d^{\omega_n}\right)} \\ &\quad\times\cos\left(\frac{\varphi_a^{\omega_n}-\varphi_b^{\omega_n}}{2}\right) \\ &\quad\times\begin{pmatrix}\mathrm{e}^{\mathrm{i}\varphi_f^{\omega_n}}\cos\left(\frac{\varphi_c^{\omega_n}-\varphi_d^{\omega_n}}{2}\right)\\ \mathrm{i}\mathrm{e}^{\mathrm{i}\varphi_e^{\omega_n}}\sin\left(\frac{\varphi_c^{\omega_n}-\varphi_d^{\omega_n}}{2}\right)\sqrt{g}\end{pmatrix} \qquad (10)\\ &= \tilde{E}_{\text{in}}(\omega_n)\cdot\tilde{\mathbf{H}}^{\text{mod}\,6}(\omega_n)\,. \qquad (11)\end{aligned}$$

Equations (8) and (10) are equal when setting $\varphi_d^{\omega_n}$ and $\varphi_f^{\omega_n}$ to zero. Due to the physical dimensions, the liquid crystals have an intrinsic offset retardance. This is not identifiable since the arrays are fixed to each other and only relative changes of the retardances matter. Therefore, it is not possible to experimentally set each individual array to zero or to a multiple of 2π. The difference retardance of $\varphi_c-\varphi_d$ is the parameter which replaces φ_c. Further, the modulation function of this setup is over-determined. It uses six arrays to control the four parameters phase, amplitude, ellipticity, and orientation. In order to reduce the number of parameters and ensure uniqueness, the following transformation is made.

$$\begin{aligned}&\varphi_a^{\omega_n}-\varphi_b^{\omega_n}=\varphi_{\text{D}ab}^{\omega_n}; \qquad &&\varphi_a^{\omega_n}+\varphi_b^{\omega_n}=\varphi_{\text{S}ab}^{\omega_n};\\ &\varphi_c^{\omega_n}-\varphi_d^{\omega_n}=\varphi_{\text{D}cd}^{\omega_n}; \qquad &&\varphi_c^{\omega_n}+\varphi_d^{\omega_n}=\varphi_{\text{S}cd}^{\omega_n}=0; \qquad (12)\\ &\varphi_e^{\omega_n}-\varphi_f^{\omega_n}=\varphi_{\text{D}ef}^{\omega_n}; \qquad &&\varphi_e^{\omega_n}+\varphi_f^{\omega_n}=\varphi_{\text{S}ef}^{\omega_n}=0.\end{aligned}$$

The formula for the six-array equation (10) setup simplifies to

$$\begin{aligned}\tilde{\mathbf{E}}_{\text{out}}^{\text{mod SD}}(\omega_n) &= \tilde{E}_{\text{in}}(\omega_n)\,\mathrm{e}^{\frac{1}{2}\mathrm{i}\varphi_{\text{S}ab}^{\omega_n}}\cos\left(\frac{\varphi_{\text{D}ab}^{\omega_n}}{2}\right) \\ &\quad\times\begin{pmatrix}\mathrm{e}^{\mathrm{i}\frac{\varphi_{\text{D}ef}^{\omega_n}}{2}}\cos\left(\frac{\varphi_{\text{D}cd}^{\omega_n}}{2}\right)\\ \mathrm{i}\mathrm{e}^{-\mathrm{i}\frac{\varphi_{\text{D}ef}^{\omega_n}}{2}}\sin\left(\frac{\varphi_{\text{D}cd}^{\omega_n}}{2}\right)\sqrt{g}\end{pmatrix} \qquad (13)\\ &= \tilde{E}_{\text{in}}(\omega_n)\cdot\tilde{\mathbf{H}}^{\text{mod SD}}(\omega_n)\,. \qquad (14)\end{aligned}$$

2.3 Calculation of the retardances for a parameterized pulse sequence

In order to transfer the retardances of the modulation function from the calculated desired field to the modulator, the frequency has to be resampled to the frequency steps of the modulator ω_n. Then, the modulation function of the desired field is identified with the modulation function of the modulator:

$$\tilde{\mathbf{H}}^{\text{par}}(\omega_n)=\tilde{\mathbf{H}}^{\text{mod}}(\omega_n)\,. \qquad (15)$$

This leads to a system of four coupled linear equations. In the case of the modulator which utilizes four arrays, we obtain

$$\begin{aligned}\text{Re}\,H_x^{\omega_n} &= \frac{1}{4}\big(\cos\big(\varphi_a^{\omega_n}+\varphi_e^{\omega_n}\big)+\cos\big(\varphi_b^{\omega_n}+\varphi_e^{\omega_n}\big)\\ &\quad+\cos\big(\varphi_a^{\omega_n}+\varphi_c^{\omega_n}+\varphi_e^{\omega_n}\big)\\ &\quad+\cos\big(\varphi_b^{\omega_n}+\varphi_c^{\omega_n}+\varphi_e^{\omega_n}\big)\big), \qquad (16)\\ \text{Im}\,H_x^{\omega_n} &= \frac{1}{4}\big(\sin\big(\varphi_a^{\omega_n}+\varphi_e^{\omega_n}\big)+\sin\big(\varphi_b^{\omega_n}+\varphi_e^{\omega_n}\big)\\ &\quad+\sin\big(\varphi_a^{\omega_n}+\varphi_c^{\omega_n}+\varphi_e^{\omega_n}\big)\\ &\quad+\sin\big(\varphi_b^{\omega_n}+\varphi_c^{\omega_n}+\varphi_e^{\omega_n}\big)\big), \qquad (17)\\ \text{Re}\,H_y^{\omega_n} &= \frac{1}{4}\big(-\cos\big(\varphi_a^{\omega_n}\big)-\cos\big(\varphi_b^{\omega_n}\big)\\ &\quad+\cos\big(\varphi_a^{\omega_n}+\varphi_c^{\omega_n}\big)\\ &\quad+\cos\big(\varphi_b^{\omega_n}+\varphi_c^{\omega_n}\big)\big)\sqrt{g}, \qquad (18)\\ \text{Im}\,H_y^{\omega_n} &= \frac{1}{4}\big(-\sin\big(\varphi_a^{\omega_n}\big)-\sin\big(\varphi_b^{\omega_n}\big)\\ &\quad+\sin\big(\varphi_a^{\omega_n}+\varphi_c^{\omega_n}\big)\\ &\quad+\sin\big(\varphi_b^{\omega_n}+\varphi_c^{\omega_n}\big)\big)\sqrt{g}. \qquad (19)\end{aligned}$$

The analogous equation system for the six-array modulator is written as

$$\begin{aligned}\text{Re}\,H_x^{\omega_n} &= \cos\left(\frac{\varphi_{\text{D}ab}^{\omega_n}}{2}\right)\cos\left(\frac{\varphi_{\text{D}cd}^{\omega_n}}{2}\right)\\ &\quad\times\cos\left(\frac{\varphi_{\text{D}ef}^{\omega_n}+\varphi_{\text{S}ab}^{\omega_n}}{2}\right), \qquad (20)\end{aligned}$$

$$\operatorname{Im} H_x^{\omega_n} = \cos\left(\frac{\varphi_{\mathrm{D}ab}^{\omega_n}}{2}\right)\cos\left(\frac{\varphi_{\mathrm{D}cd}^{\omega_n}}{2}\right) \times \sin\left(\frac{\varphi_{\mathrm{D}ef}^{\omega_n} + \varphi_{\mathrm{S}ab}^{\omega_n}}{2}\right), \tag{21}$$

$$\operatorname{Re} H_y^{\omega_n} = \cos\left(\frac{\varphi_{\mathrm{D}ab}^{\omega_n}}{2}\right)\sin\left(\frac{\varphi_{\mathrm{D}cd}^{\omega_n}}{2}\right) \times \sin\left(\frac{\varphi_{\mathrm{D}ef}^{\omega_n} - \varphi_{\mathrm{S}ab}^{\omega_n}}{2}\right)\sqrt{g}, \tag{22}$$

$$\operatorname{Im} H_y^{\omega_n} = \cos\left(\frac{\varphi_{\mathrm{D}ab}^{\omega_n}}{2}\right)\sin\left(\frac{\varphi_{\mathrm{D}cd}^{\omega_n}}{2}\right) \times \cos\left(\frac{\varphi_{\mathrm{D}ef}^{\omega_n} - \varphi_{\mathrm{S}ab}^{\omega_n}}{2}\right)\sqrt{g}. \tag{23}$$

Both systems of linear equations can be solved for the retardances. The solution for the four-array modulator is

$$\varphi_a^{\omega_n} = \pm\mathrm{ACOS} - \mathrm{ACOT} - \mathrm{ATAN}, \tag{24}$$

$$\varphi_b^{\omega_n} = \mp\mathrm{ACOS} - \mathrm{ACOT} - \mathrm{ATAN}, \tag{25}$$

$$\varphi_c^{\omega_n} = 2\,\mathrm{ACOT}, \tag{26}$$

$$\varphi_e^{\omega_n} = \mathrm{ACOTX} + \mathrm{ATAN}. \tag{27}$$

For $\varphi_a^{\omega_n}$ and $\varphi_b^{\omega_n}$, two solutions can be found, which are indicated by $\pm$ and $\mp$, respectively.

Similarly, the sums and differences of the retardances of the setup which utilizes six arrays can be found:

$$\varphi_{\mathrm{S}ab}^{\omega_n} = \mathrm{ACOTX} - \mathrm{ATAN}, \tag{28}$$

$$\varphi_{\mathrm{D}ab}^{\omega_n} = \pm 2\,\mathrm{ACOS}, \tag{29}$$

$$\varphi_{\mathrm{D}cd}^{\omega_n} = 2\,\mathrm{ACOT}, \tag{30}$$

$$\varphi_{\mathrm{D}ef}^{\omega_n} = \mathrm{ACOTX} + \mathrm{ATAN}. \tag{31}$$

For a shortened and clearly laid out presentation, the following abbreviations have been used:

$$\mathrm{ACOS} = \arccos\left(\sqrt{1 + \frac{(\operatorname{Im} H_x^{\omega_n})^2}{(\operatorname{Re} H_x^{\omega_n})^2}}\operatorname{Re} H_x^{\omega_n}\sqrt{1 + \frac{(\operatorname{Im} H_y^{\omega_n})^2 + (\operatorname{Re} H_y^{\omega_n})^2}{((\operatorname{Im} H_x^{\omega_n})^2 + (\operatorname{Re} H_x^{\omega_n})^2)\ g}}\right), \tag{32}$$

$$\mathrm{ACOT} = \operatorname{arc\,cot}\left(\frac{\sqrt{1 + \frac{(\operatorname{Im} H_x^{\omega_n})^2}{(\operatorname{Re} H_x^{\omega_n})^2}}\operatorname{Re} H_x^{\omega_n}\operatorname{Im} H_y^{\omega_n}\sqrt{1 + \frac{(\operatorname{Re} H_y^{\omega_n})^2}{(\operatorname{Im} H_y^{\omega_n})^2}}\sqrt{g}}{(\operatorname{Im} H_y^{\omega_n})^2 + (\operatorname{Re} H_y^{\omega_n})^2}\right), \tag{33}$$

$$\mathrm{ACOTX} = \operatorname{arc\,cot}\left(\frac{\operatorname{Re} H_x^{\omega_n}}{\operatorname{Im} H_x^{\omega_n}}\right), \tag{34}$$

$$\mathrm{ATAN} = \arctan\left(\frac{\operatorname{Re} H_y^{\omega_n}}{\operatorname{Im} H_y^{\omega_n}}\right). \tag{35}$$

An obligatory condition derives from energy conservation. The shaped pulse which leaves the setup cannot have a higher pulse energy than the one which enters the setup. So, $|\tilde{\mathbf{E}}_{\mathrm{out}}(\omega_n)| \le |\tilde{\mathbf{E}}_{\mathrm{in}}(\omega_n)|$ is valid for all ω_n.

Since the first two arrays control the spectral amplitude, the retardances of these arrays ($\varphi_a^{\omega_n}$, $\varphi_b^{\omega_n}$, or $\varphi_{\mathrm{D}ab}^{\omega_n}$) become complex if this condition is violated. Therefore, the spectral amplitude has to be normalized to fulfill this condition. Including the grating correction in the equations in which the parameter g takes the difference in reflectivity into account leads to a slightly different normalization. Again, the correction focuses on the parameters of the first arrays. This difference is controlled by the term within the arc cos function, which can be reformulated to

$$\sqrt{\left(\operatorname{Re} H_x^{\omega_n}\right)^2 + \left(\operatorname{Im} H_x^{\omega_n}\right)^2 + \frac{(\operatorname{Im} H_y^{\omega_n})^2 + (\operatorname{Re} H_y^{\omega_n})^2}{g}}.$$

This term can be identified as the absolute value of the modulation function. Its value must be smaller than unity because the liquid crystal arrays can only attenuate and not increase the intensity of light. This is achieved by renormalization of the overall intensity of the desired pulse sequence.

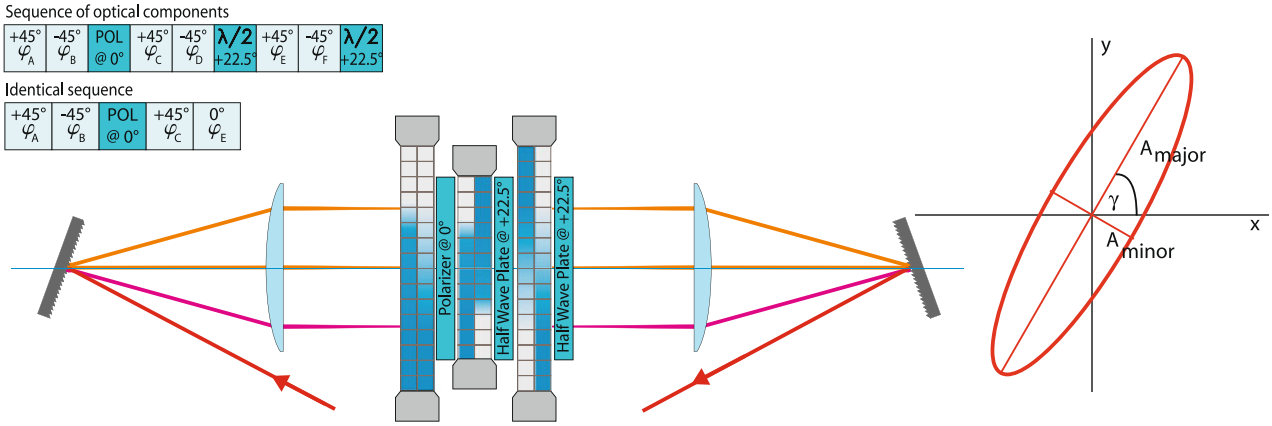

Fig. 1 Pulse shaper setup for full control of phase, amplitude, and polarization of femtosecond laser pulses. For the modulation of the pulses, three standard double liquid crystal array modulators, a polarizer, and a pair of half-wave plates are used. They are placed in the Fourier plane of a 4-f line in the order shown in the inset on the *upper left*. This device provides the same control as the sequence of four liquid crystal arrays. The inset on the *right* shows a polarization ellipse with its major (A_{major}) and minor (A_{minor}) axes. The orientation is described by the angle γ

3 Experimental setup

The experimental setup of the pulse shaper is presented in Fig. 1. The laser pulses are modulated in the Fourier plane of a 4-f line. It consists of two cylindrical lenses with a focal length of 200 mm and two gratings with 1200 grooves/mm having a polarization-dependent difference in reflectivity of 15% for horizontally and vertically polarized light. Since a four-array modulator is not available, we use three standard double liquid crystal modulators (2× SLM1280 and SLM-256, CRi) having their optical axes oriented at ±45°, a polarizer, and two wave plates. This is discussed in detail in [17]. Each modulator is mounted on a high-precision stage to coordinate the pixel assignment and adjust them to match the same frequency band ω_n. The wavelength calibration coefficient for the arrays amounts to 0.3415 nm/pixel.

The femtosecond laser pulses are provided by an oscillator (Mira, Coherent) with a bandwidth of 22 nm centered at 780 nm. The pulses are detected by sum-frequency-generation cross correlation (SFG-XC) in a BBO crystal with a short reference pulse. Due to the high polarization sensitivity of the SFG, different projections of the shaped pulse can be selected by rotating the shaped pulse with a half-wave plate. In a time resolved ellipsometry like scheme the three-dimensional pulse shape is retrieved using the cross-correlation traces at 10 different projection angles [11, 19].

4 Systematic variation of a single parameter

In this section, we experimentally demonstrate the functionality of the parameterization in combination with the introduced setup which uses six arrays. To prove that it is possible to control each parameter of every individual sub-pulse, we generated and measured a series of double pulses. These pulses were retrieved. This provides information of the polarization parameters' orientation and ellipticity evolution as well as intensity over time. The intensity graph which basically is the integrated SFG-XC signal reveals directly the distance and chirp of the measured pulse. For a systematic investigation, we varied a single parameter of the double-pulse sequence while keeping the others constant. The particular parameter under investigation is plotted. The same parameter of the other pulse is additionally plotted to serve as a reference. To illustrate this scan, we exemplarily choose two pulses out of each series to show the evolution of the intensity and the polarization parameters. This is presented along with a three-dimensional representation of the pulse. Figure 2 depicts the variation of the sub-pulse energy. In Fig. 3 the distance of the double pulse is changed. By chirping the first pulse linearly, one can observe an elongation of its pulse duration while the second pulse remains short. This is depicted in Fig. 4. A variation of the polarization parameters can be observed in the following two figures. In Fig. 5 the second pulse is rotated by maintaining its linear polarization. The change of the ellipticity of the second sub-pulse is depicted in Fig. 6. Statistics regarding the remaining parameters which were kept constant are presented in Table 1.

This set of measurements nicely showed the prospects of this setup. The graphs in part (a) of Figs. 2–6 proved that the selected parameter can individually be controlled. As expected, the points all lie on a straight line. In the case of the chirp, the dependence of the width of the peak in the cross-correlation trace is not linear, which is correct and shows the expected characteristics. The graphs representing the intensity, ellipticity, and orientation as well as the three-dimensional representation of the measured pulse revealed that by changing the particular parameters the overall shape

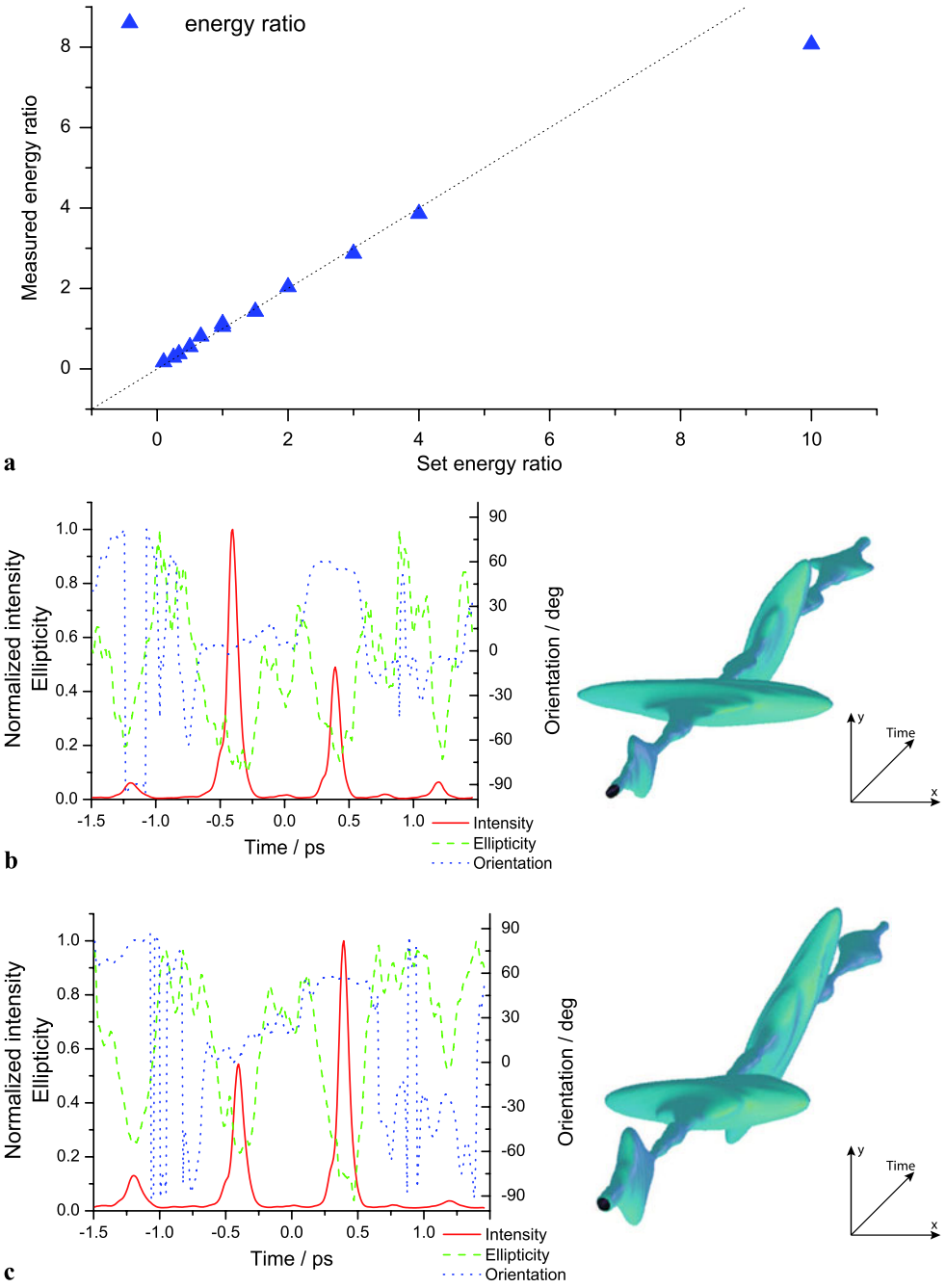

Fig. 2 Variation of the sub-pulses' energy. (**a**) shows the change of the relative energy between the two pulses from 1:10 to 10:1. The other sub-pulse parameters are kept constant. Both pulses are linearly polarized. The first pulse is oriented at 0° and the second at +60°. The distance between the sub-pulses amounts to 800 fs. In (**b**) and (**c**) the energy ratio amounts to 2. In (**b**) the first pulse has twice the energy of the second. In (**c**) it is the other way round

remains unchanged. However, slight deviations can be observed in the ellipticity. Furthermore, some pulses show side pulses which are not seen in the simulation of the pulses. The origin of these deviations will be discussed in Sect. 6 later in this paper.

5 Complex multi-pulses

The last section showed the systematic control of the individual parameters. In this section, we want to extend the parametrically shaped pulse sequences to complex multi-pulses. A selection of multi-pulses should give an impression of how complex the pulses shaped by this method could be. Each pulse is presented in a graph which shows the intensity, orientation, and ellipticity over time. It is accompanied by the three-dimensional representation of the pulse sequence which is reconstructed from the measured data.

The first example pulse (depicted in Fig. 7a) is a single pulse with a changing polarization state. It is constructed by superimposing two circular sub-pulses with different helic-

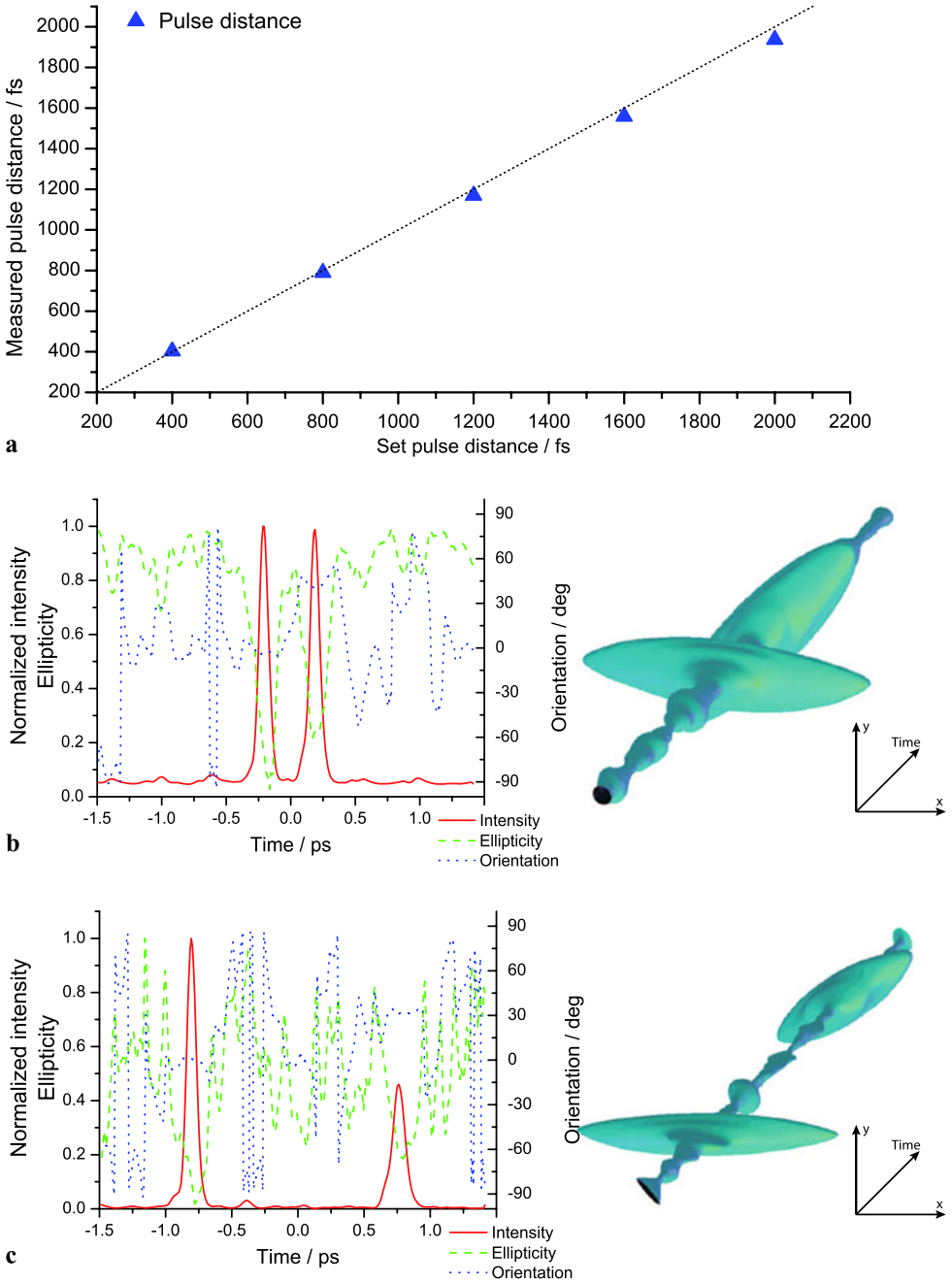

Fig. 3 Variation of the distance between the sub-pulses from 400 fs to 2000 fs. The double pulse consists of two linear sub-pulses. The first is orientated horizontally and the second at +45°. In example (**b**) the distance is set to 400 fs and in (**c**) to 1600 fs

ities. They are both linearly chirped by $+1.5 \times 10^4$ fs^2 and separated by 200 fs. This results in a rotation of the polarization ellipse of the pulse by more than 360°. The ellipticity decreases with increasing intensity and is close to linear at the pulse maximum.

The second example pulse (depicted in Fig. 7b) is a triple pulse consisting of three linear pulses oriented at −60°, 0°, and +60° which are separated in time by 300 fs. The first pulse and the last pulse are quadratically chirped by $\pm 2 \times 10^6$ fs^3. This results in the characteristic asymmetric shape in time. The pulse in between remains short.

The third example pulse is presented in Fig. 7c. The pulse sequence consists of four linearly polarized pulses separated by 200 fs. The orientation changes by 45° from sub-pulse to sub-pulse.

The last example pulse (depicted in Fig. 7d) is a pulse sequence of six short sub-pulses spaced by 200 fs. The orientation of each sub-pulse is changing from 0° to +150° in steps of 30°. Additionally, the ellipticity of each sub-pulse is increasing from linear ($r = 0.0$) to circular ($r = 1.0$) in steps of 0.2.

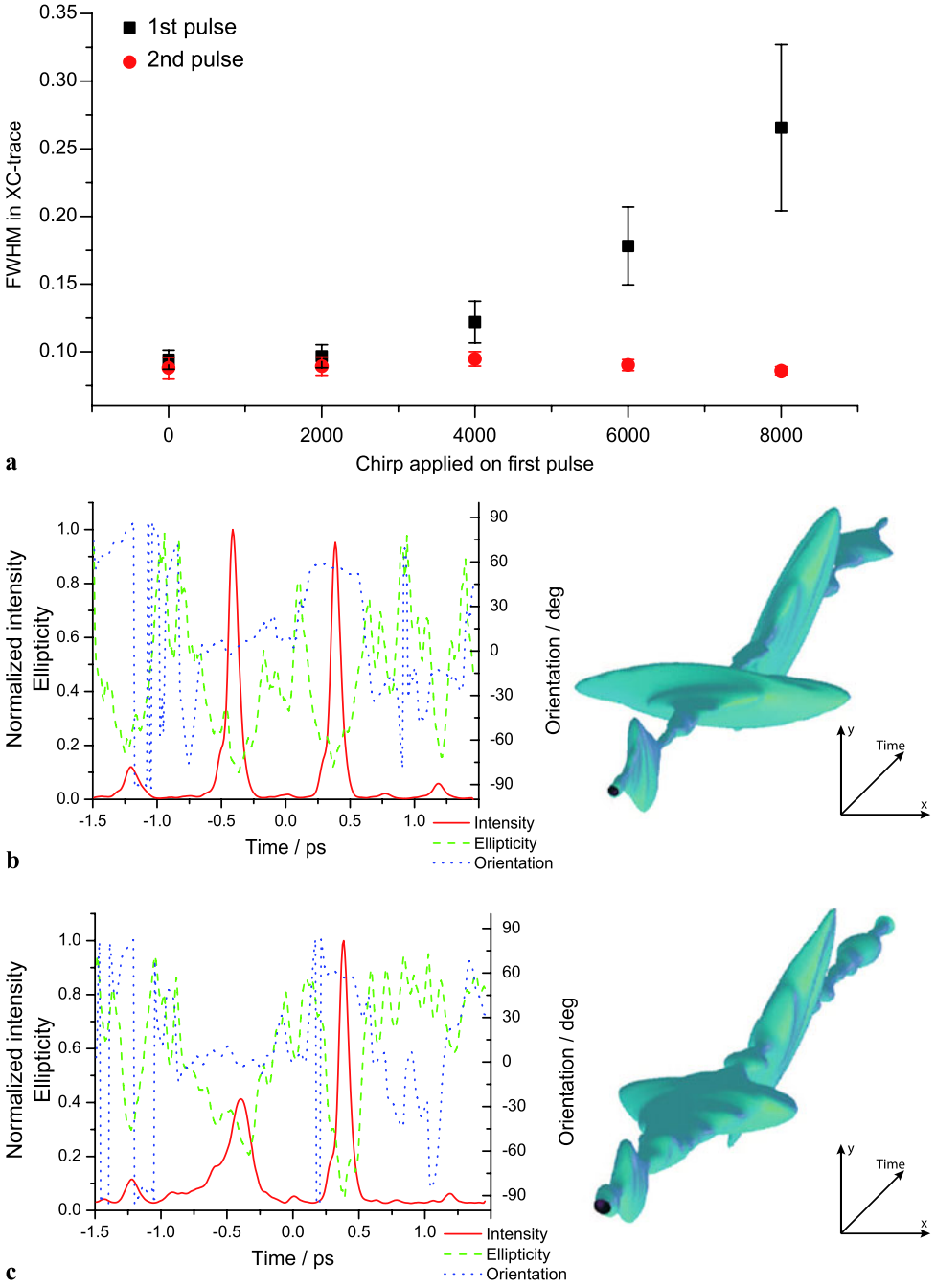

Fig. 4 In this series the effect of applying a linear chirp to the first pulse is demonstrated. The intensity trace of every curve is fitted with a Gaussian. The FWHM of the pulses' cross-correlation trace is plotted in (**a**). The pulse length would be obtained by deconvolution with the reference pulse. The length of the first pulse increases with larger chirps and the peak intensity is reduced, while the duration remains constant at about 90 fs for the second pulse. The first pulse is linearly polarized at 0° and the second linearly polarized at +60°. The pulse distance is set to 800 fs. In (**b**) the example of two short pulses is depicted. In (**c**) the first pulse is chirped by +6000 fs^2

6 Discussion

The complexity of the produced pulse shapes is limited by the provided laser bandwidth and the resolution of the modulator. Further issues which have an impact on the shape of the pulses originate from the liquid crystal modulators' technique. These are known as pixel quantization, gap-to-stripe ratio, and phase resolution, which restrict the temporal shaping window and create pulse replicas and other side effects [20, 21]. In addition, imperfections of the setup affect the produced pulses. These result from the imperfections in the optical elements, their alignment, or, especially, in the case of the liquid crystal arrays, from their calibration. To estimate the impact of the errors, we carried out simulations. Noise on the retardances and an imperfect alignment of the axes result in a less precise control of the pulse parameters. These deviations occur in the order of the error which provoked them. As any other detection method, the one which is used is afflicted by errors.

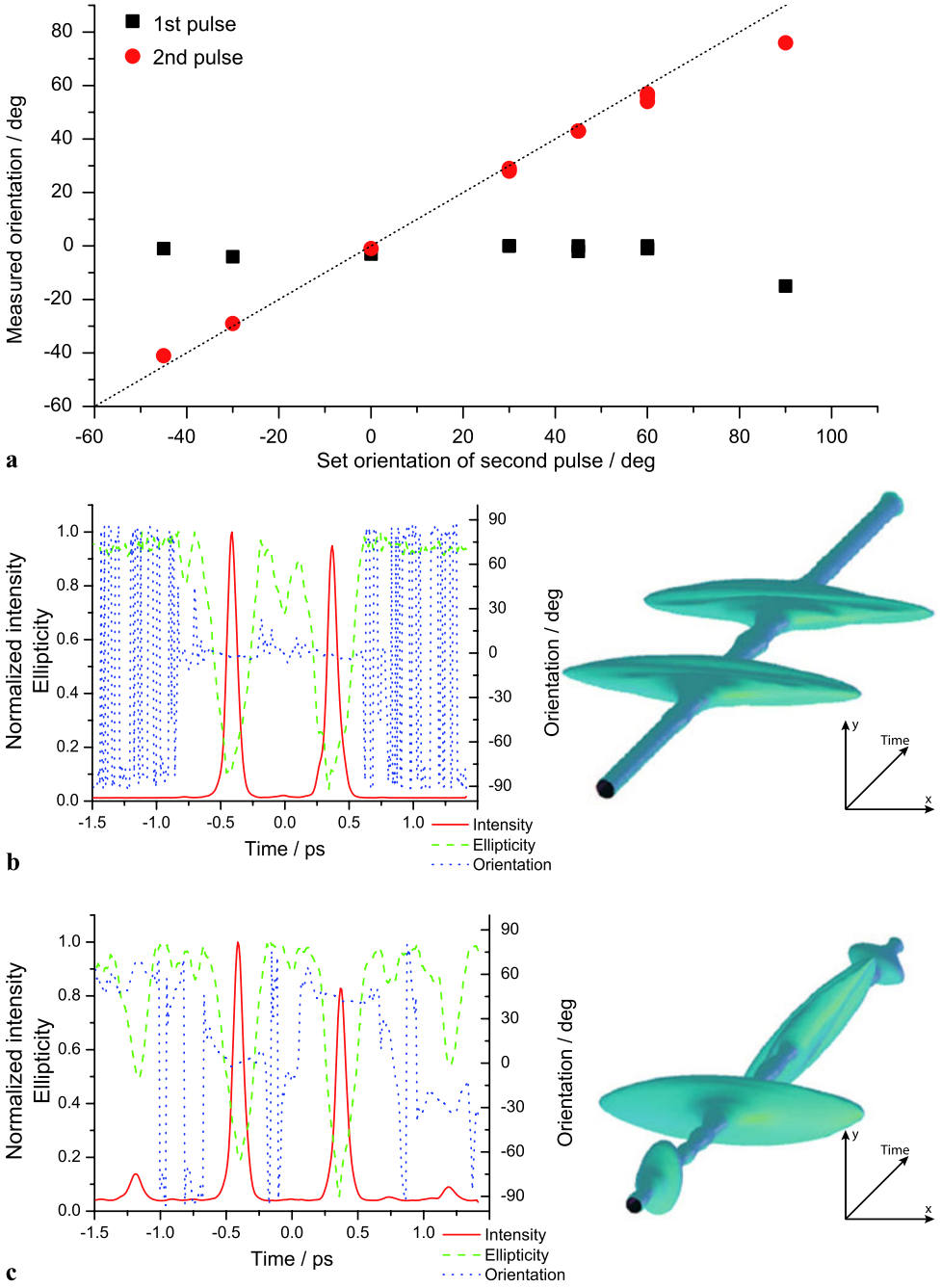

Fig. 5 The variation of the orientation is demonstrated in (**a**). The two sub-pulses have the same energy, are linearly polarized, and are separated by 800 fs. The first sub-pulse is fixed at 0°, whereas the orientation of the second sub-pulse is rotated counter clockwise. Two examples of this series are shown in (**b**) and (**c**), in which the orientation of the second sub-pulse is 0° and +45°, respectively

A more crucial point is the pixel overlap in all the succeeding arrays. A simulation of this error reveals: if every nth pixel does not precisely modulate the same frequency band, ω_n side pulses will occur. These side pulses can be observed in some of the pulses presented before. As an example, we choose the double pulse already presented in Fig. 6c. The side pulses including their polarization state are well reproduced by this simulation, which can be observed in Fig. 8. In the experiment this might be due to using three modulators—one of these being of a different type.

7 Conclusion and outlook

In conclusion, we have presented a shaper setup which is capable of phase, amplitude, and polarization shaping in combination with an analytical parametrical sub-pulse encoding. The electrical field of the generated pulse which could be designed in the time or frequency domain is only restricted by the resolution of the shaper and the available bandwidth. Since the modulation is based on the use of birefringent liquid crystals, the usable range of wavelengths is limited to their transparency, which ranges from 400 to 1600 nm. We

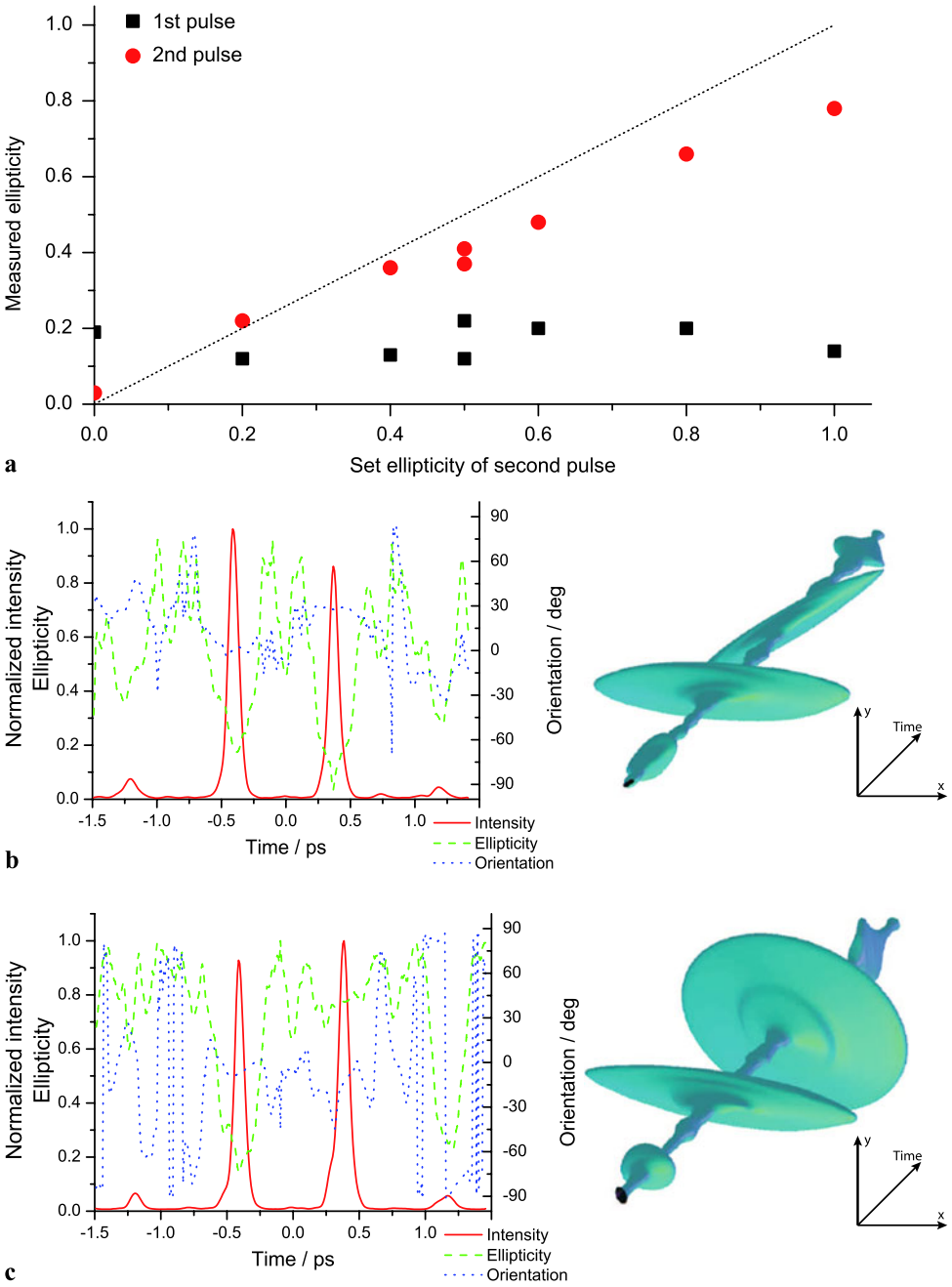

Fig. 6 In this part the variation of the ellipticity is illustrated. A double pulse which is separated by 800 fs and equal sub-pulse energies serves as an example. The orientation of the first pulse is 0° and of the second one +30°. The ellipticity of the first pulse is kept linear whereas the ellipticity of the second pulse is varied from linear ($r = 0.0$) via elliptical to circular ($r = 1.0$). In (**b**) the two sub-pulses are linearly polarized. In (**c**) the linear sub-pulse is followed by a circular one

have introduced a way to calculate the individual retardances for the arrays of the modulator from a given field. The calculations were carried out for two types of modulators: one modulator utilizing four arrays and—since this type of modulator was not available—the modulator we used in the experiment which utilizes six arrays.

Further, we employed this analytical procedure for constructing parametric pulse sequences. The pulse sequence is constructed out of sub-pulses. In this way, each sub-pulse can be individually shaped by setting its physically relevant parameters energy, position in time, ellipticity, and orientation, as well as the relative phase and higher-order chirps. To illustrate this method in combination with the introduced setup, we have generated example pulses. To characterize the pulse, we retrieved the intensity, orientation, and ellipticity over time from a set of cross-correlation traces. In order to visualize the pulses and make them more easily comprehensible, a three-dimensional representation is calculated from the measured data. We presented a series of double pulses to confirm the independent control of the parameters of each sub-pulse. In each series one of the parameters was manipulated while the other parameters were kept constant. The respective parameter of the measured pulse matches the value which was set. After hav-

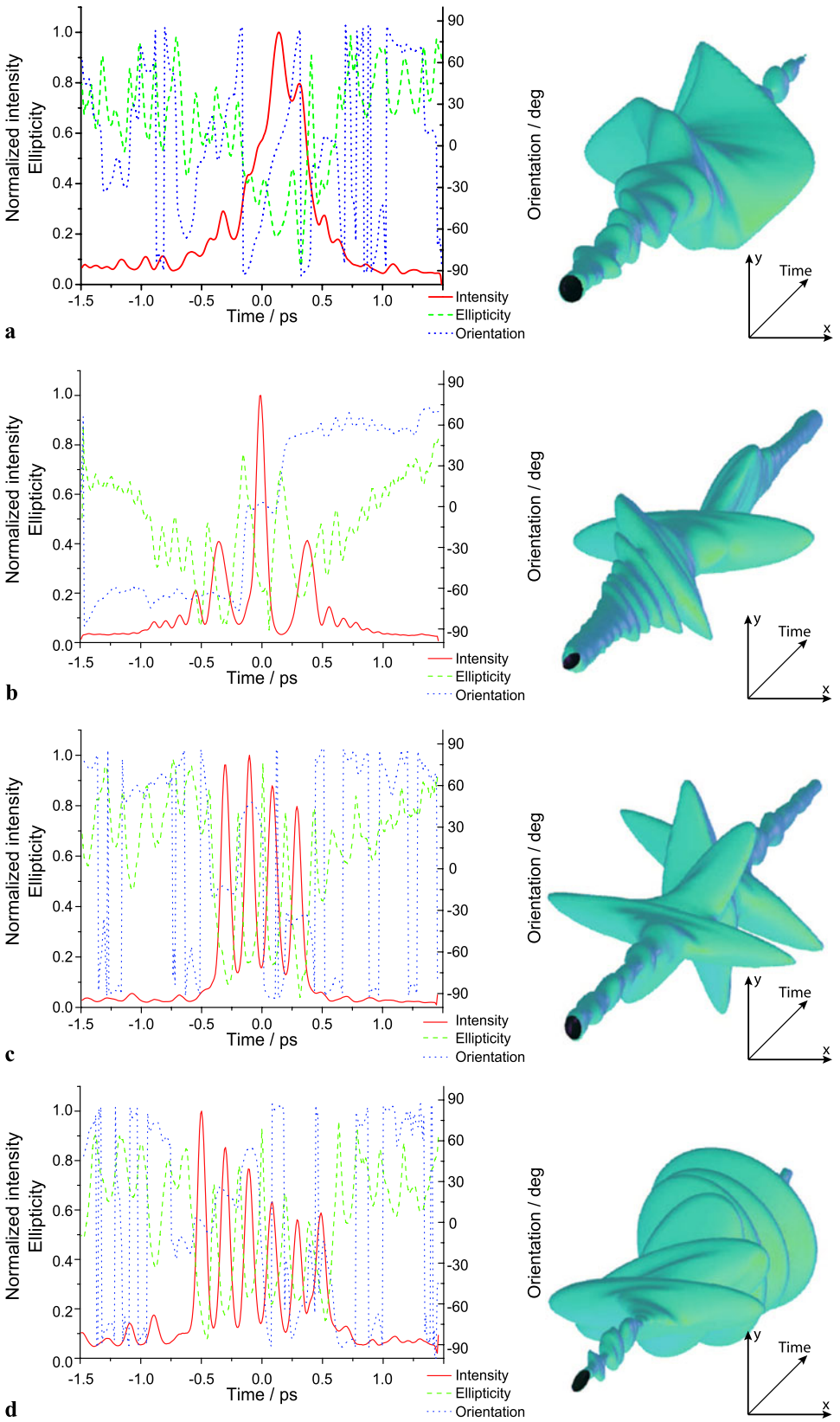

Fig. 7 Complex multi-pulses with different polarization states and chirps. The time-dependent intensity, orientation, and ellipticity, as well as the three-dimensional representation, are depicted. All are retrieved from measured XC data.

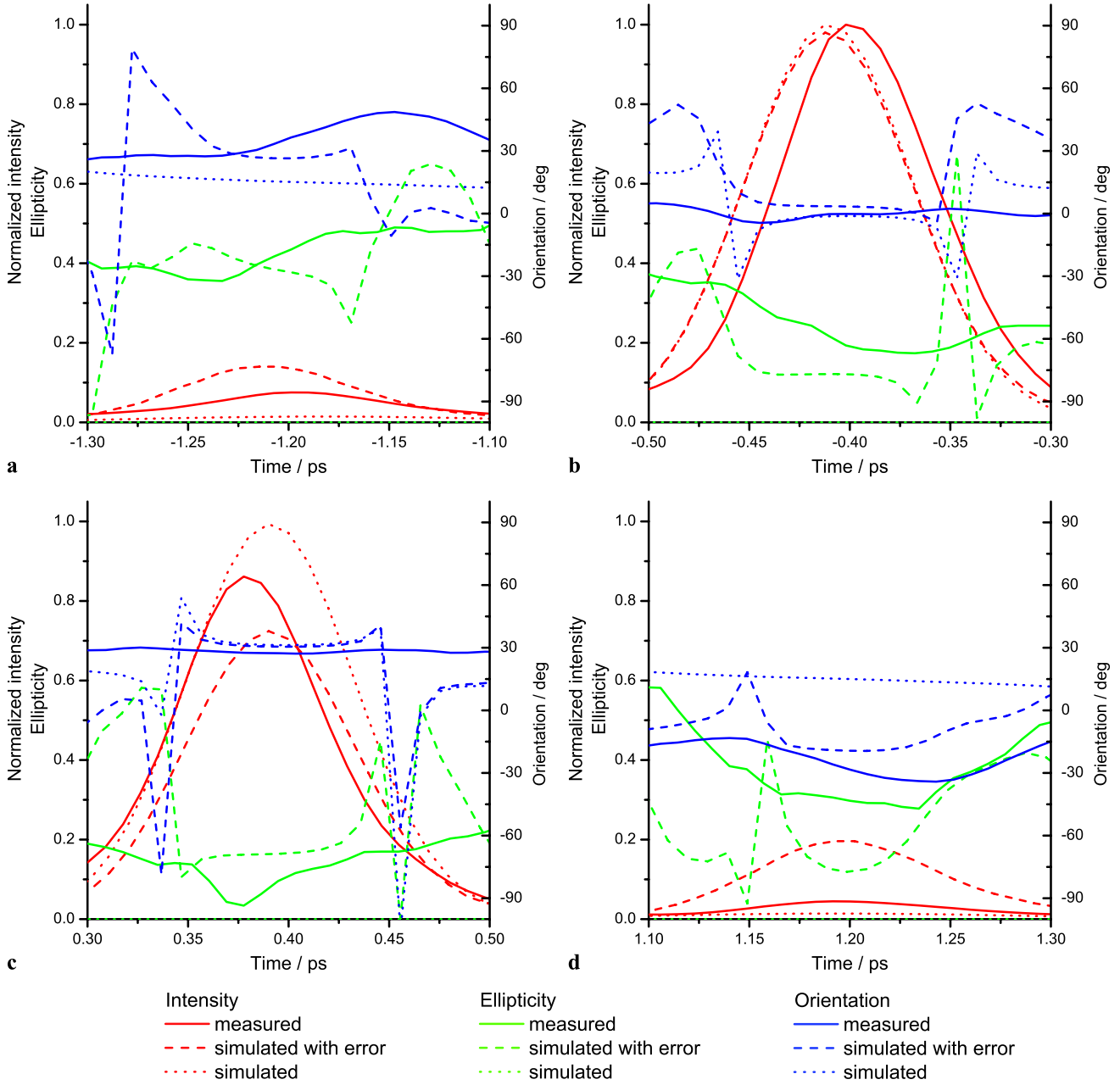

Fig. 8 A theoretical investigation of the deviations in the pulse sequence induced by shifting the first double array by one pixel relative to the others. The double pulse from Fig. 6b serves as an example. It consists of two linearly polarized pulses separated by 800 fs and orientated at 0° and +30°. The sub-pulses which are intended and the ones which are due to the error are investigated separately in (**a**)–(**d**). The intensity (*red*), ellipticity (*green*), and orientation (*blue*) over time are plotted for each sub-pulse. Each graph of the measured pulse (*solid line*) is compared to the simulated one with (*dashed line*) and without (*dotted line*) error. The graph resulting from the experiment is very similar to the one obtained by simulation, in which a shift of one pixel on the first double array is applied

ing proven the ability to control the sub-pulses arbitrarily, more complex pulses were shown. The limitations of this setup and potential sources of errors are discussed. These parametrically tailored pulses can be employed for systematic investigation by separately changing one parameter of a pulse sequence, for example in two-dimensional spectroscopy. Furthermore, the implementation of this procedure in the algorithms of feedback loop optimizations would tremendously decrease the size of the search space, which results in fast convergence and higher reproducibility. The obtained pulse shapes are less complex and, due to the employment of physically concrete parameters, they are easier to interpret [22, 23]. In summary, the application of these parametrically shaped three-dimensional pulses could have

Table 1 Parameters of the double pulses which are depicted in Figs. 2–6. Each column represents a series of double pulses. The set parameters and statistics on measured parameters which are kept constant in the respective series are displayed

	Shown in	Intensity Fig. 2	Distance Fig. 3	Chirp Fig. 4	Orientation Fig. 5	Ellipticity Fig. 6
Energy ratio	Set	Varied	1.0	1.0	1.0	1.0
	Measured		1.5 ± 0.5	0.8 ± 0.2	1.2 ± 0.2	1.0 ± 0.1
Distance	Set	800 fs	Varied	800 fs	800 fs	800 fs
	Measured	796 ± 3 fs		798 ± 16 fs	785 ± 10 fs	788 ± 7 fs
Pulse length	Set	Short	Short	Varied	Short	Short
First pulse	Measured	92 ± 1 fs	83 ± 1 fs		89 ± 4 fs	85 ± 4 fs
Pulse length	Set	Short	Short	Short	Short	Short
Second pulse	Measured	83 ± 1 fs	95 ± 1 fs	105 ± 3 fs	90 ± 2 fs	93 ± 2 fs
Orientation	Set	0°	0°	0°	0°	0°
First pulse	Measured	$+2 \pm 6°$	$-2 \pm 2°$	$0 \pm 5°$	$-2 \pm 4°$	$-7 \pm 3°$
Orientation	Set	+60°	+45°	+60°	Varied	+30°
Second pulse	Measured	$+56 \pm 1°$	$+38 \pm 6°$	$+55 \pm 3°$		$+14 \pm 13°$
Ellipticity	Set	0.00	0.00	0.00	0.00	0.00
First pulse	Measured	0.20 ± 0.09	0.21 ± 0.11	0.24 ± 0.06	0.18 ± 0.06	0.16 ± 0.04
Ellipticity	Set	0.00	0.00	0.00	0.00	Varied
Second pulse	Measured	0.17 ± 0.04	0.21 ± 0.06	0.17 ± 0.06	0.14 ± 0.09	

a positive impact on many experiments in quantum control.

Acknowledgements The authors thank Prof. Ludger Wöste for support as well as Dr. Stefan M. Weber and Dr. Mateusz Plewicki for stimulating discussions. This work was supported by the Deutsche Forschungsgemeinschaft in the frame of the Sonderforschungsbereich 450.

References

1. A.M. Weiner, D.E. Leaird, J.S. Patel, J.R. Wullert, Opt. Lett. **15**, 326 (1990)
2. D. Goswami, Phys. Rep. **374**, 385 (2003)
3. R.S. Judson, H. Rabitz, Phys. Rev. Lett. **68**, 1500 (1992)
4. P. Nuernberger, G. Vogt, T. Brixner, G. Gerber, Phys. Chem. Chem. Phys. **9**, 2470 (2007)
5. T. Brixner, G. Gerber, Opt. Lett. **26**, 557 (2001)
6. T. Brixner, G. Krampert, T. Pfeifer, R. Selle, G. Gerber, M. Wollenhaupt, O. Graefe, C. Horn, D. Liese, T. Baumert, Phys. Rev. Lett. **92**, 208301 (2004)
7. T. Suzuki, S. Minemoto, T. Kanai, H. Sakai, Phys. Rev. Lett. **92**, 133005 (2004)
8. L. Polachek, D. Oron, Y. Silberberg, Opt. Lett. **31**, 631 (2006)
9. H. Miao, A.M. Weiner, L. Mirkin, P.J. Miller, Opt. Lett. **32**, 2360 (2007)
10. M. Plewicki, S.M. Weber, F. Weise, A. Lindinger, Appl. Phys. B **86**, 259 (2007)
11. M. Plewicki, F. Weise, S.M. Weber, A. Lindinger, Appl. Opt. **45**, 8356 (2006)
12. M. Ninck, A. Galler, T. Feurer, T. Brixner, Opt. Lett. **32**, 3379 (2007)
13. O. Masihzadeh, P. Schlup, R.A. Bartels, Opt. Express **15**, 18025 (2007)
14. M. Sato, T. Suzuki, K. Misawa, Rev. Sci. Instrum. **80**, 123107 (2009)
15. C.T. Middleton, D.B. Strasfeld, M.T. Zanni, Opt. Express **17**, 14526 (2009)
16. P. Nuernberger, R. Selle, F. Langhojer, F. Dimler, S. Fechner, G. Gerber, T. Brixner, J. Opt. A **11**, 085202 (2009)
17. F. Weise, A. Lindinger, Opt. Lett. **34**, 1258 (2009)
18. S.M. Weber, F. Weise, M. Plewicki, A. Lindinger, Appl. Opt. **46**, 5987 (2007)
19. G.E. Jellison Jr., D.H. Lowndes, Appl. Phys. Lett. **47**, 718 (1985)
20. A.M. Weiner, D.E. Leaird, J.S. Patel, J.R. Wullert, IEEE J. Quantum Electron. **28**, 908 (1992)
21. A.M. Weiner, Prog. Quantum Electron. **19**, 161 (1995)
22. S.M. Weber, A. Lindinger, F. Vetter, M. Plewicki, A. Merli, L. Wöste, Eur. Phys. J. D **33**, 39 (2005)
23. T. Hornung, R. Meier, M. Motzkus, Chem. Phys. Lett. **326**, 445 (2000)